

Bayesian Inference for PDE-based Inverse Problems using the Optimization of a Discrete Loss

Lucas Amoudruz^a, Sergey Litvinov^a, Costas Papadimitriou^b, Petros Koumoutsakos^a

^a*Computational Science and Engineering Laboratory Harvard John A. Paulson School of Engineering and Applied Sciences
19 Oxford St Cambridge MA 02138 United States.*

^b*System Dynamics Laboratory Department of Mechanical Engineering University of Thessaly Volos 38334 Greece*

Abstract

Inverse problems are crucial for many applications in science, engineering and medicine that involve data assimilation, design, and imaging. Their solution infers the parameters or latent states of a complex system from noisy data and partially observable processes. When measurements are an incomplete or indirect view of the system, additional knowledge is required to accurately solve the inverse problem. Adopting a physical model of the system in the form of partial differential equations (PDEs) is a potent method to close this gap. In particular, the method of optimizing a discrete loss (ODIL) has shown great potential in terms of robustness and computational cost. In this work, we introduce B-ODIL, a Bayesian extension of ODIL, that integrates the PDE loss of ODIL as prior knowledge and combines it with a likelihood describing the data. B-ODIL employs a Bayesian formulation of PDE-based inverse problems to infer solutions with quantified uncertainties. We demonstrate the capabilities of B-ODIL in a series of synthetic benchmarks involving PDEs in one, two, and three dimensions. We showcase the application of B-ODIL in estimating tumor concentration and its uncertainty in a patient's brain from MRI scans using a three-dimensional tumor growth model.

Keywords: Inverse problems, Bayesian inference, ODIL, Partial Differential Equations

1. Introduction

Inverse problems are ubiquitous in science, engineering, and medicine, in particular for problems where observations provide only indirect or incomplete information about a system [1]. Inverse problems are central in a wide range of applications such as flow field reconstruction [2, 3, 4], data assimilation [5], medical imaging [6, 7], and parameters estimation of material properties [8, 9, 10]. A particularly challenging class of inverse problems arises when the forward model is governed by ordinary differential equations (ODEs) or partial differential equations (PDEs) [11]. Incorporating physical knowledge through mathematical models constrains the space of admissible solutions and can reduce the severity of ill-posedness, although inverse problems often remain ill-posed and still require regularization [12, 13, 14]. However, this approach can suffer from the high dimensionality of the problem, stiffness, noisy measurements, and sensitivity to parameters. In particular, quantifying the uncertainties of solutions is challenging with standard techniques for inverse PDE problems such as Bayesian inference [15, 14], variational methods [16], ensemble Kalman methods [17], and adjoint-based optimization [18], which can be limited with issues of scalability, robustness, and computational cost. Bayesian inference for PDE-constrained inverse problems, Laplace and Gauss-Newton-type approximations, has been extensively studied in the context of function-space formulations [14, 19, 20, 21].

In parallel, operator learning approaches based on DeepONets [22], Fourier neural operators [23], and graph neural networks [24, 25] have been extended to inverse problems and uncertainty quantification [26, 27, 28]. Similar Bayesian techniques rely on training data to build prior knowledge [29]. However, the application of these operator learning techniques to large-scale problems is limited by the cost of their training and the difficulty of generating sufficient high-fidelity data. In addition, their performance can degrade when the

training data do not cover the regimes encountered in the inverse problem, making their generalization challenging.

More recently, PDE-based inverse problems were solved with the methods of physics-informed neural networks (PINNs) [30] and optimizing a discrete loss (ODIL) [31]. In both these approaches, the solution of the inverse problem is obtained by minimizing a loss that contains two terms: the deviation between the field and the data, and the residuals of the PDE evaluated at collocation points in space-time. Combining these terms into a single loss was pioneered by Leeuwen and Herrmann and applied to linear PDEs [18]. PINNs and ODIL differ in their representation of the field and in the way PDE residuals are estimated. PINNs represent the field as the output of a neural network that has space-time as its input. Residuals of the PDE are then estimated through automatic differentiation. In contrast, fields in ODIL are stored on a grid, and PDE residuals are estimated using traditional discretizations, leading to a considerable computational advantage over PINNs because of the locality of these operators [31]. PINNs and ODIL have been successful in many applications ranging from fluid mechanics [32, 4, 33, 34] to tumor growth [35, 36] and learning policies for fluid control and manipulation [37, 38].

Despite these advances, PINNs and ODIL solutions can be affected by measurement errors of the provided data. In particular, it is not clear how these measurement errors affect the uncertainties of the solution of the inverse problem. Recent studies have addressed these issues in the context of PINNs [39, 40] through a Bayesian and a conformal prediction framework [41] approach to account for the variability of the unknown field. However, a similar theory has not been developed for ODIL. We note that the Bayesian extensions of PINNs have been applied to problems of less than two dimensions. On the other hand, a Bayesian extension of ODIL could potentially provide quantified uncertainties for inverse problems in higher dimensions, as ODIL was shown to be orders of magnitude faster and more robust than PINNs in two and three dimensional benchmark problems [31].

In this study, we present B-ODIL, a Bayesian extension of ODIL. B-ODIL enables uncertainty quantification and robustness to model error in high-dimensional PDE-based inverse problems, while retaining the computational structure and scalability of ODIL. In this framework, the prior incorporates knowledge from the PDE, while the likelihood couples the observed data to the unknown field. This method provides a solution to the inverse problem with quantified uncertainties. We account for the computational burden by estimating the posterior distribution with different sampling techniques and two approximation strategies: (i) a full Laplace approximation to the joint posterior for moderate-dimensional problems, and (ii) a parameter-focused mode approximation designed for scalable inference in large-scale cases. We have designed a series of benchmarks with increasing levels of complexity to test B-ODIL. First, we consider the ODE describing the dynamics of a harmonic oscillator, to compare the validity of the Laplace and mode approximations compared with Hamiltonian Monte-Carlo (HMC) sampling of the same posterior in a computationally tractable setting. We then apply B-ODIL to the one dimensional PDE of the diffusion equation with unknown initial conditions, introducing the challenge of ill-posed inverse problems, typical in PDE-based inference, where uncertainty quantification is crucial. The third benchmark tests the method’s ability to reconstruct the states of a non-linear two dimensional PDE from synthetic data, and we demonstrate that the ground truth falls within the uncertainty bounds provided by B-ODIL. Finally, we apply the method to a three dimensional model of tumor growth coupled with real patients data, and provide estimates of tumor cell fields with quantified uncertainties given medical images.

2. Methods

2.1. ODIL

We consider a PDE defined in the space-time domain Ω with boundaries and initial conditions on $\partial\Omega$,

$$\begin{aligned} \mathcal{L}(\mathbf{u}, \theta) &= 0, & \text{in } \Omega, \\ \mathcal{B}(\mathbf{u}, \theta) &= 0, & \text{on } \partial\Omega, \end{aligned} \tag{1}$$

where \mathcal{L} is a differential operator that encodes the PDE, \mathcal{B} encodes the boundary and initial conditions, \mathbf{u} is the unknown field and θ are the parameters of the model. Discretizing over space and time into a grid,

we can solve the discrete version of eq. (1):

$$\begin{aligned}\mathcal{L}_i^h(\mathbf{u}, \theta) &= 0, & i = 1, \dots, N, \\ \mathcal{B}_j^h(\mathbf{u}, \theta) &= 0, & j = 1, \dots, N_B,\end{aligned}\tag{2}$$

where \mathcal{L}^h and \mathcal{B}^h are the discretized versions of \mathcal{L} and \mathcal{B} , respectively, and \mathbf{u} is the unknown discretized field. To solve the discretized problem, we can reformulate eq. (2) as a minimization of the loss

$$L_{\text{PDE}}(\mathbf{u}, \theta) = \frac{1}{N} \sum_{i=1}^N \mathcal{L}_i^h(\mathbf{u}, \theta)^2 + \frac{1}{N_B} \sum_{j=1}^{N_B} \mathcal{B}_j^h(\mathbf{u}, \theta)^2,\tag{3}$$

where N and N_B are the number of discrete components of the discretized operators \mathcal{L}^h and \mathcal{B}^h , respectively. In the setting of an inverse problem, parts of the problem description such as initial conditions and boundary conditions may be missing and need to be estimated from measurements. Given these measurements $\{y_k\}_{k=1}^{N_D}$ and the corresponding measurement operators $h_k(\mathbf{u}, \theta)$, $k = 1, 2, \dots, N_D$, the inverse problem can be solved by minimizing the loss

$$L(\mathbf{u}, \theta) = L_{\text{PDE}}(\mathbf{u}, \theta) + \frac{\lambda}{N_D} \sum_{k=1}^{N_D} (y_k - h_k(\mathbf{u}, \theta))^2,\tag{4}$$

where λ is a positive constant that describes the importance of fitting the data with respect to satisfying the discrete PDE. In this work, the minimization of eq. (4) is performed with gradient-based methods implemented in Pytorch [42] and detailed in the results section.

2.2. B-ODIL: Bayesian inference for inverse problems with ODIL

We now consider the Bayesian formulation of PDE-based inverse problems, where the goal is to infer parameters θ and the solution field \mathbf{u} from noisy measurements $\mathcal{D} = \{y_k\}_{k=1}^{N_D}$, given a model in the form of a PDE. In this framework, the posterior distribution is obtained by combining a likelihood model for the data with prior knowledge enforcing compatibility between the solution field and the PDE. As we have seen in the previous section, ODIL provides a natural way to encode this compatibility through a PDE loss. We thus incorporate this PDE loss into the prior information, allowing us to extend ODIL into the Bayesian setting. In classical Bayesian inverse problems with well-posed PDEs and accurate forward models, one often eliminates the state variable via a map $\mathbf{u} = f(\theta)$, yielding a reduced posterior over θ . In contrast, B-ODIL targets settings in which the governing equations are enforced approximately through a residual-based term and may be affected by discretization error or model misspecification. In this regime, enforcing a strict parameter-to-state map can lead to biased and overconfident posteriors, motivating the use of a joint posterior over (\mathbf{u}, θ) that can accommodate structural model error. We assume that the measurements \mathcal{D} are noisy and that we have a model describing this noise. We would like to estimate the parameters θ and the solution \mathbf{u} , with quantified uncertainties. According to the Bayes' theorem, the posterior distribution of these quantities given the data reads

$$P(\mathbf{u}, \theta | \mathcal{D}) \propto P(\mathcal{D} | \mathbf{u}, \theta)P(\mathbf{u}, \theta),\tag{5}$$

where we omit the normalization constant $P(\mathcal{D})$. The term $P(\mathbf{u}, \theta)$ denotes the prior knowledge of the parameters and solution field, and $P(\mathcal{D} | \mathbf{u}, \theta)$ is the likelihood of the data. A common form of the likelihood assumes that the observations are statistically independent and that they are normally distributed:

$$P(\mathcal{D} | \mathbf{u}, \theta) = \prod_{k=1}^{N_D} \frac{1}{\sqrt{2\pi\sigma^2}} \exp\left(-\frac{(y_k - h_k(\mathbf{u}, \theta))^2}{2\sigma^2}\right),\tag{6}$$

where σ is the standard deviation associated with the observable and h_k , $k = 1, \dots, N_D$, are measurement operators on the solution \mathbf{u} . For example, h_k can be a linear interpolation of the field at the measurement location from the discrete field \mathbf{u} . Throughout this work, measurements are assumed conditionally independent

given (\mathbf{u}, θ) , corresponding to independent observation noise; correlations between measurements could be incorporated through a non-diagonal likelihood covariance but are not considered here for simplicity. Other likelihood models can be used within the same framework. Examples are provided in the results section.

As prior knowledge, we assume that the possible solutions \mathbf{u} are compatible with the PDE associated with the model. To account for this knowledge, the prior over the solution \mathbf{u} with parameters θ is such that the loss $L_{\text{PDE}}(\mathbf{u}, \theta)$ is small, and thus we choose priors of the form

$$P(\mathbf{u}, \theta) = \frac{1}{Z} \exp(-\beta L_{\text{PDE}}(\mathbf{u}, \theta)) P(\theta), \quad (7)$$

where β is a positive scalar that controls how peaked the distribution is, and Z is a normalization constant that does not depend on \mathbf{u} or θ . Finally, $P(\theta)$ contains additional prior knowledge on θ . In this work, $P(\theta)$ is taken as improper uniform prior in all cases. The prior in eq. (7) is defined at the discrete level through the loss L_{PDE} . As a result, the posterior is a discretization-dependent object. In this work we adopt a computational perspective and evaluate posterior stability under mesh refinement (see section 3.1), which provides an empirical check that discretization effects are negligible once posterior summaries have converged. We refer to Stuart [14], Cotter et al. [43] for the function-space formulation of Bayesian inverse problems and discretization-robust algorithms. The posterior distribution of the solution and parameters of the model thus becomes

$$P(\mathbf{u}, \theta | \mathcal{D}) \propto P(\mathcal{D} | \mathbf{u}, \theta) \frac{1}{Z} \exp(-\beta L_{\text{PDE}}(\mathbf{u}, \theta)) P(\theta). \quad (8)$$

The dimensionality of this problem is large due to the unknown variables \mathbf{u} , challenging sampling techniques. To obtain tractable uncertainty estimates in high dimensions, we use the Laplace approximation to the joint posterior. The log-posterior reads

$$\log P(\mathbf{u}, \theta | \mathcal{D}) = \log P(\mathcal{D} | \mathbf{u}, \theta) - \beta L_{\text{PDE}}(\mathbf{u}, \theta) - \log Z + \log P(\theta) + C, \quad (9)$$

where C is a scalar that does not depend on θ or \mathbf{u} . We expand this quantity in Taylor series up to second order around the maximum a posteriori (MAP), where the linear term vanishes, leading to the Laplace approximation [44]

$$\log P(\mathbf{v} | D) \approx \log P(\mathbf{v}^* | D) + \frac{1}{2} (\mathbf{v} - \mathbf{v}^*)^T H (\mathbf{v} - \mathbf{v}^*), \quad (10)$$

where $\mathbf{v} = (\mathbf{u}, \theta)$, \mathbf{v}^* is the solution at the MAP, and H is the Hessian of the log-posterior evaluated at \mathbf{v}^* . Thus, the posterior is approximated with a multivariate Gaussian with mean \mathbf{v}^* and covariance $\Sigma = -H^{-1}$. As with any local Gaussian approximation, the Laplace method is expected to be inaccurate for strongly non-Gaussian or multimodal posteriors. In such regimes, full sampling or alternative approximations would be required. We note that when the likelihood takes the form of eq. (6), maximizing eq. (9), i.e. finding the MAP, corresponds to the original ODIL method, eq. (4) with $\lambda = N_D/\beta$, assuming that $P(\mathbf{u})$ and $P(\theta)$ are taken as improper uniform priors. Thus, computing uncertainties over predictions that were computed with ODIL consists only in computing the Hessian and inverting it. In general, forming and inverting the Hessian with respect to $\mathbf{v} = (\mathbf{u}, \theta)$ is computationally prohibitive when \mathbf{u} is high-dimensional; consequently, the full Laplace approximation is feasible only for relatively low-dimensional benchmarks, while large-scale problems require parameter-focused or reduced approximations discussed below.

2.3. Inference of model parameters for inverse problems

In the previous section we formulated a posterior distribution based on the prior knowledge that contains information about the PDE (eq. (7)) and on the likelihood of observing the data (eq. (6)) that fits well with the ODIL formulation. This results in a joint posterior distribution for the unknown field \mathbf{u} and the model parameters θ . This distribution typically lies on a large-dimensional space, and it becomes quickly intractable to sample from this distribution. Similarly, in large dimensions, obtaining the Laplace approximation is costly, as the computation of the Hessian of the posterior increases quadratically with

the size of the problem. In some cases, we are only interested in the posterior distribution of the model parameters, which can be obtained by marginalizing over \mathbf{u} :

$$P(\theta|\mathcal{D}) = \int P(\mathbf{u}, \theta|\mathcal{D})d\mathbf{u}. \quad (11)$$

The evaluation of this high-dimensional integral is intractable. Instead, we assume that the joint distribution is peaked around the MAP $\mathbf{u}^*(\theta) = \arg \max_{\mathbf{u}} P(\mathbf{u}|\theta, \mathcal{D})$ and we approximate the posterior distribution of the model parameters using the mode approximation [44]

$$P(\theta|\mathcal{D}) \approx P(\mathbf{u}^*(\theta), \theta|\mathcal{D}). \quad (12)$$

In practice, the dimensionality of θ is small compared to that of \mathbf{u} . Thus, sampling from eq. (12) can be performed with traditional sampling methods such as Markov chain Monte-Carlo (MCMC) or transitional Markov chain Monte-Carlo (TMCMC), where each sample involves an optimization problem with respect to \mathbf{u} .

The formulation adopted here is not intended as a replacement for classical Bayesian inference based on repeated forward model evaluations under a strict parameter-to-state map $\mathbf{u} = f(\theta)$. Such reduced formulations are appropriate when the forward model is accurate and can be evaluated efficiently for each value of θ . In contrast, B-ODIL targets settings in which the governing equations may be misspecified. We note that several studies have approached this problem by directly altering the model [45] or by statistically correcting its output [46]. Here, we instead incorporate the PDE residual as a soft probabilistic constraint in the prior. Embedding optimization over \mathbf{u} within inference over θ allows the PDE constraints and the data to be reconciled at the field level, while the parameter β controls tolerance to model error. As shown in section 3.2, this is essential for obtaining calibrated posteriors under misspecification, where standard Bayesian inference can otherwise become overconfident and biased.

2.4. Selection of the parameter β

The parameter β controls the relative importance of the PDE-residual prior and the data likelihood. When the governing equations are known to be accurate, large values of β enforce strong adherence to the model. The limit $\beta \rightarrow \infty$ corresponds to classical methods for PDE-based Bayesian inverse problems. In the presence of model error or misspecification, however, overly large β can lead to biased and overconfident posterior estimates.

In practice, β can be selected in different ways depending on the availability of data and computational resources. A principled approach consists in selecting β by maximizing the predictive log-likelihood on held-out data. Specifically, the available observations are split into training and validation sets. For each candidate value of β , B-ODIL is applied to the training data to obtain a posterior distribution, which is then evaluated on the validation data. The value β^* maximizing the validation log-likelihood is retained.

When validation is impractical (e.g., limited data or high computational cost), we select β by tuning, guided by the same trade-off as in classical ODIL and by posterior diagnostics (e.g., predictive uncertainty and residual structure). Alternatively, β can be treated as a hyperparameter and selected by maximizing the model evidence, at the cost of introducing a prior on β and additional approximation or optimization steps. In the present work we primarily use cross-validation when feasible, and otherwise adopt pragmatic tuning that is consistent with ODIL practice and supported by posterior predictive checks.

3. Results

We demonstrate the applicability of this method by first illustrating its application to simple problems such as the Harmonic Oscillator and the diffusion equation. We then proceed to examine the formulation for the reaction-diffusion equations and then its application to estimate uncertainties of a tumor concentration field given observed magnetic resonance imaging (MRI) data of real patients.

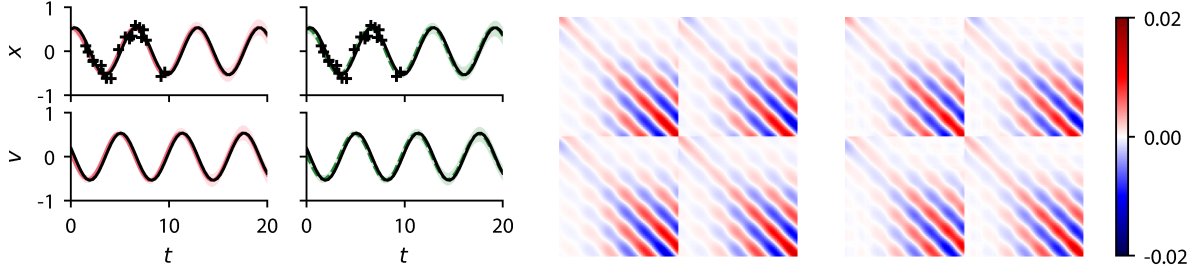


Figure 1: Left: Prediction of the position (top row) and velocity (bottom row) of the oscillator given the data (crosses) using the B-ODIL framework with Laplace approximation (left column) and HMC (right column). The shaded area denotes the 5 to 95% quantiles of the posterior, and the solid line denotes the posterior mean. The dashed line represents the underlying process that was used to generate the data. Right: Covariance matrices of the full solution $(x_1, \dots, x_N, v_1, \dots, v_N)$ obtained from the Laplace approximation (left column) and estimated from HMC samples (right column).

3.1. Harmonic oscillator

We first consider a simple example to demonstrate the validity of the Laplace approximation and that of eq. (12). Consider the system of ODEs of a harmonic oscillator with position x , velocity v , mass m and spring coefficient k ,

$$\frac{dx}{dt} = v, \quad (13)$$

$$\frac{dv}{dt} = -\frac{k}{m}x, \quad (14)$$

for time $t \in (0, T)$ and with unknown initial conditions. Given measurements of position at known times $\mathcal{D} = \{t_j, x_j\}_{j=1}^{N_D}$ with known standard deviation σ , we want to predict the position and velocity of the system throughout the whole time interval. We discretize the position and velocity into $N = 64$ equidistant time intervals with $\Delta t = T/N$ and $T = 20$. The discrete losses are computed using the midpoint rule,

$$\mathcal{L}_i^h(\mathbf{x}, \mathbf{v}) = \left(\frac{x_{i+1} - x_i}{\Delta t} - \frac{v_{i+1} + v_i}{2}, \frac{v_{i+1} - v_i}{\Delta t} + \frac{k}{m} \frac{x_{i+1} + x_i}{2} \right). \quad (15)$$

Finally, the observation functions correspond to linear interpolations of the positions at data points t_j , $j = 1, 2, \dots, N_D$. For now, we assume that the parameter $\omega = \sqrt{k/m} = 1$ is known. We use synthetic data consisting of $N_D = 20$ time points uniformly distributed in $t \in (0, T/2)$, and corresponding positions with Gaussian distribution centered around the exact solution of the model with standard deviation of $\sigma = 0.1$. The initial conditions used to generate the data were set to $x(0) = 0.5$ and $v(0) = 0.2$. We choose a value of $\beta = 10^4$ in the prior distribution (see eq. (7)). The MAP is computed by maximizing the posterior with respect to (\mathbf{x}, \mathbf{v}) with the Adam optimizer [47] with learning rate 10^{-3} for 10'000 epochs. Computing the Laplace approximation for this case takes about 2 s on a consumer-grade laptop. The Laplace approximation of this problem is shown on fig. 1. For comparison, we solve the same problem with HMC on the same posterior, and show the results on the same figure. The HMC results were obtained from a custom implementation of the original HMC algorithm [48] with 10'000 samples, chain lengths $l = 10$, mass matrix $M = 1$, and step size $\delta t = 0.008$, tuned for an acceptance rate of $\alpha \approx 0.65$. This implementation with these parameters took about 5 min on a consumer-grade laptop.

With both Laplace and HMC approaches, the uncertainties increase away from the data that was used to calibrate the model. Furthermore, these uncertainties are similar between both methods, despite the Gaussian approximation in the Laplace approach. To compare the methods, we show the correlation matrix of the entries in the discretized solution (\mathbf{x}, \mathbf{v}) on fig. 1. In the Laplace approach, this quantity corresponds to the inverse of the Hessian matrix of the log-posterior distribution. With HMC, we estimate this matrix

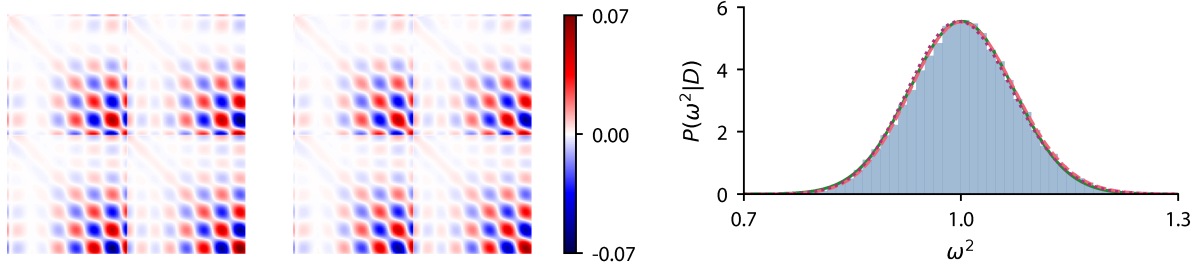


Figure 2: Left: Covariance matrices of the posterior distribution of the full solution $(\omega^2, x_1, \dots, x_N, v_1, \dots, v_N)$ obtained with the Laplace and HMC methods. Right: Marginal posterior probability of ω^2 obtained from HMC (histogram), Laplace (solid line), mode approximation given by eq. (12) (dashed line), and exact solution (dots).

by computing the empirical correlation between samples. The correlation matrices obtained from the two methods are close to each other, indicating that the Laplace approximation gives a good representation of the posterior distribution.

We also consider the same problem but with an unknown value of ω . The procedure for the Laplace approach and HMC sampling are the same as above except that now we also infer the model parameter $\theta = \omega^2 = k/m$. The covariance matrices of the vector $(\omega^2, \mathbf{x}, \mathbf{v})$ are shown in fig. 2 and have a very similar structure. In addition, we estimate the marginal distribution of the model parameter ω using the approximation given by eq. (12), evaluated at 50 equally spaced points for $0.7 \leq \omega \leq 1.3$. The marginal distribution of ω^2 is shown in fig. 2. For the Laplace approximation, this distribution corresponds to a Gaussian with mean around the MAP $(\omega^*)^2$ and variance $(H^{-1})_{\omega^2, \omega^2}$. The HMC, Laplace and mode approximations show excellent agreement with the exact solution, centered around the reference value $\omega^2 = 1$ that was used to generate the data. The exact solution is obtained by expanding eq. (11), noting that the logarithm of the joint density of \mathbf{u}, θ is quadratic in \mathbf{u} for a fixed θ . Thus, for a fixed $\theta = \omega^2$,

$$\log P(\mathbf{u}, \theta | \mathcal{D}) = l(\mathbf{u}^*(\theta), \theta) + \frac{1}{2}(\mathbf{u} - \mathbf{u}^*(\theta))^T H(\theta)(\mathbf{u} - \mathbf{u}^*(\theta)),$$

where l is the log-likelihood, $\mathbf{u}^*(\theta) = \arg \max_{\mathbf{u}} l(\mathbf{u}, \theta)$, and $H(\theta)$ is the Hessian matrix of l with respect to \mathbf{u} , evaluated at $\mathbf{u}^*(\theta)$. Replacing this expression into eq. (11), we get

$$P(\theta | \mathcal{D}) = \frac{(2\pi)^{d/2}}{\sqrt{\det H(\theta)}} \exp l(\mathbf{u}^*(\theta), \theta),$$

where d is the dimension of \mathbf{u} . To evaluate this expression for each value of θ , we use the optimal value $\mathbf{u}^*(\theta)$ estimated with ODIL, and use automatic differentiation in Pytorch to compute $H(\theta)$. We use this approach throughout this work. In practice, $\mathbf{u}^*(\theta)$ is obtained by numerical optimization and is therefore only approximate; the resulting expression should be interpreted as a Laplace-type approximation based on a locally quadratic expansion around a numerically converged solution.

Finally, we study the effect of the grid size N and parameter β . First we fix the PDE weight $\beta = 10^4$ and the number of measurements $N_D = 20$, and predict the position x at the last grid point ($t = 20$) given the data and the discretized PDE. Figure 3 shows that the posterior of $x(t = 20)$ converges as we increase the grid size. In practice, and throughout this work, we select the smallest grid resolution for which posterior summaries have converged, in order to minimize computational cost while avoiding discretization-induced artifacts.

Second, we vary the parameter β for three values of N_D and with a fixed resolution $N = 256$, for which the posterior has converged. The variance of the posterior prediction of x at time $t = 20$ is shown against β in fig. 3. For each value of N_D , we observe two regimes. For low values of β , corresponding to soft priors on the model, the variance decreases linearly with β . When β is large, the variance reaches a plateau that is

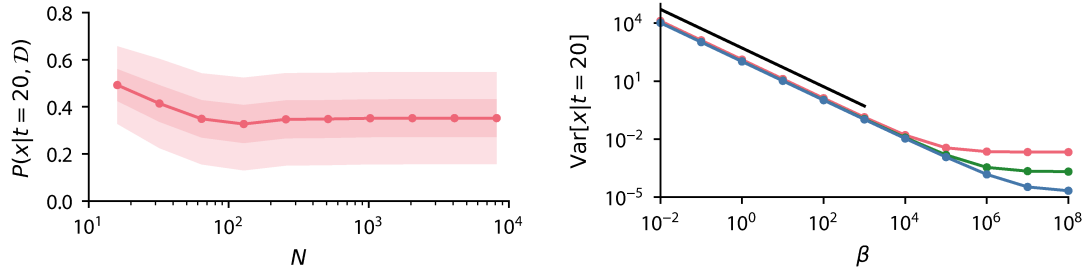


Figure 3: Left: Prediction of the position x at time $t = 20$ with the Laplace approximation against the grid size n_t . Symbols represent the mean prediction and shaded areas represent the 50% and 90% confidence intervals. Right: Variance of the prediction of x at time $t = 20$ against the parameter β , with $N_D = 10, 100$, and 1000 , from top to bottom. The solid black line shows a linear decrease with β .

limited by the uncertainties coming from the data term. As expected, a larger amount of data N_D decreases the value of this plateau. In the limit $\beta \rightarrow \infty$, the discretized PDE is enforced exactly, and thus the only uncertainties come from the data. Empirically, larger β values increase the conditioning of the optimization problem and the number of iterations required for convergence, without improving predictions once the posterior variance has reached the data-limited plateau. We thus use values of β that are smaller than the start of the plateau. From a Bayesian perspective, β controls the tolerance to model error by tempering the influence of the PDE-based prior relative to the data likelihood. In many practical cases, we do not know models that are perfectly consistent with observations, in which case a lower value of β is favored. We give more details about this choice in the next section.

3.2. Choice of the parameter β under model misspecification

We now illustrate the practical impact of the β -selection strategy introduced in section 2.4 in a setting with deliberate model misspecification. Specifically, we consider a variation of the harmonic oscillator example from section 3.1, in which the data are generated by an unknown nonlinear oscillator while inference is performed using the linear model. The nonlinear oscillator follows the dynamics

$$\frac{dx}{dt} = v, \quad (16)$$

$$\frac{dv}{dt} = -\frac{1}{m}(k_1x + k_2x^3), \quad (17)$$

where k_1 and k_2 are positive constants. We generate $N_D = 200$ data points using $x_0 = 2$, $v_0 = 0$, $m = 15$, $k_1 = 1$, $k_2 = 2$, and noise $\sigma = 0.4$. We then apply the B-ODIL framework with the linear model described by eq. (15), using the Adam optimizer with a learning rate of 5×10^{-4} over 50000 epochs. This procedure mimics many practical cases where the statistical model is an approximation of the true underlying data generation process. We split the data into training and validation sets (80% and 20% of the data, respectively), run B-ODIL on the training set with different values of β , and select β^* by maximizing the validation log-likelihood.

Figure 4 shows the log-likelihood of the validation set against β . High values of β result in a plateauing log-likelihood, as the method tends to conventional Bayesian inference as $\beta \rightarrow \infty$. On the other hand, low values of β lead to a decrease of the log-likelihood as the model is less and less trusted to make sharp predictions. This log-likelihood has a maximum around $\beta^* \approx 5.7$, which balances fitting the data and trusting the model. We use this value to make predictions and show the posterior distribution of the position and the velocity in fig. 4. The 90% confidence intervals of the posterior contain the true underlying process. In contrast, conventional Bayesian inference based on the misspecified linear model produces overly concentrated posteriors that fail to account for structural model error, leading to confidence intervals that do not capture the true dynamics away from the data (fig. 4). This result was obtained with the MCMC sampling method with 100'000 samples and a proposal step size tuned to have a 35% acceptance rate.

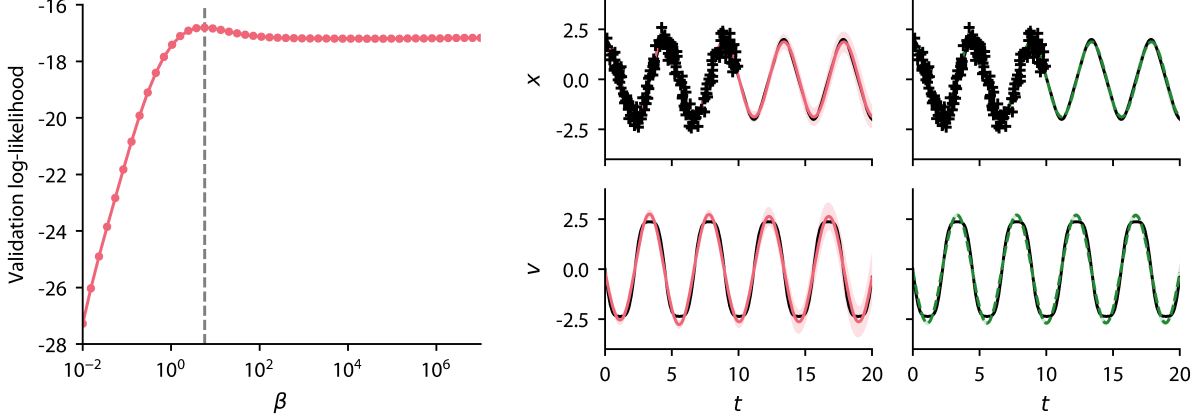


Figure 4: Predictions of and oscillator dynamics with a linear spring model with data coming from a nonlinear spring. Left: log-likelihood of the validation set against the parameter β . We select the value β^* that maximizes this log-likelihood. Right: Posterior prediction of the position and velocity field with the B-ODIL framework with $\beta = \beta^*$ (left column), and with conventional Bayesian inference (right column). The solid black line shows the exact underlying process used to produce the data.

3.3. Diffusion equation

We now consider the one-dimensional diffusion equation with a known diffusion coefficient $D = 0.1$, described by the PDE

$$\frac{\partial u}{\partial t} - D \frac{\partial^2 u}{\partial x^2} = 0, \quad \text{on } (0, L) \times (0, T), \quad (18)$$

with periodic boundary conditions and unknown initial conditions. We generate a synthetic dataset of $N_D = 200$ measurements of the field u at uniformly sampled locations in space-time, $\mathcal{D} = \{x_i, t_i, u_i\}_{i=1}^{N_D}$, with Gaussian noise of known magnitude $\sigma = 0.1$ (fig. 5). The data is generated with initial conditions $u(x, 0) = \cos(2\pi x/L)$. We want to infer the field u given this dataset \mathcal{D} and eq. (18).

We first discretize eq. (18) with finite differences on a uniform grid,

$$\mathcal{L}^h(\mathbf{u})_i^n = \frac{u_i^{n+1} - u_i^n}{\Delta t} - D \frac{u_{i-1}^{n+\frac{1}{2}} - 2u_i^{n+\frac{1}{2}} + u_{i+1}^{n+\frac{1}{2}}}{\Delta x^2} = 0, \quad (19)$$

where $u_i^n \approx u(x_i, t_n)$ with $x_i = i\Delta x$ and $t_n = n\Delta t$. Furthermore, we have defined $u_i^{n+\frac{1}{2}} = (u_i^{n+1} + u_i^n)/2$, $\Delta x = L/n_x$, and $\Delta t = T/n_t$. We set $L = 1$, $n_x = 16$, $T = 1$ and $n_t = 64$. Following eq. (9), the posterior distribution of \mathbf{u} is given by

$$\log P(\mathbf{u}|\mathcal{D}) = - \sum_{k=1}^{N_D} \frac{(u_k - \mathbf{u}_{i_k}^{n_k})^2}{2\sigma^2} - \frac{N_D}{2} \log 2\pi\sigma^2 - \frac{\beta}{N} \sum_{i=1}^N (\mathcal{L}_i^h(\mathbf{u}))^2, \quad (20)$$

where we have set $\beta = 10^4$. We compute the MAP by maximizing eq. (20) using the LBFGS optimizer [49] as implemented in PyTorch. Each call to the optimizer performs up to 20 internal quasi-Newton iterations with a strong Wolfe line search. We run 500 such optimization steps, retaining a curvature history of size 100 throughout. The initial step size is set to 5×10^{-4} . Computing the Laplace approximation for this case takes about 10s on a consumer-grade laptop. This inverse problem is ill-posed because the initial conditions are unknown and the diffusion process is inherently not time reversible [11]. Thus, many different initial states can produce indistinguishable noisy measurements at later times. The MAP associated with eq. (19) is shown on fig. 5, and we can observe deviations between the inferred field at $t = 0$ and the initial conditions used to generate the dataset. This deviation is expected at early times, as explained above.

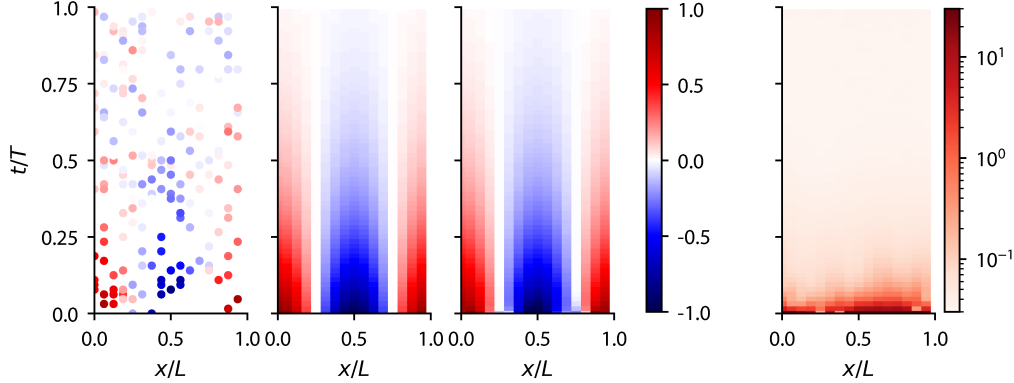


Figure 5: Laplace approximation applied to the diffusion equation. From left to right: Data used for inferring the field; Exact solution, used to generate the data; MAP solution of the diffusion problem given the data; spread of uncertainty given by the Laplace approximation (5-95% quantiles).

In order to obtain uncertainties of \mathbf{u} , we apply the Laplace method to eq. (20). We note that since eq. (20) is quadratic in \mathbf{u} , the Laplace method is exact in this case. Figure 5 shows the predicted uncertainties of the field u . At time $t = 0$, the uncertainties are large compared to the magnitude of the field. This is again expected since inferring initial conditions is an ill-posed problem in this case. In contrast, at larger times, the uncertainties over u are much lower (about 3×10^{-2}), consistent with the fact that data at previous times reduced the range of possible values at larger times. We remark that in this 1024-dimensional space setting, sampling with HMC was unsuccessful. The solution with the Laplace approach is exact so HMC sampling was not needed, but this suggests that in the next sections, where the dimension of the problems are much larger, HMC sampling is unlikely to be successful. Thus, we ignore this approach in the rest of this study.

3.4. Reaction-diffusion equation

We consider the reaction-diffusion PDE on the time-space domain $\Omega = [0, L] \times [0, L] \times [0, T]$,

$$\frac{\partial u}{\partial t} = \nabla \cdot (D \nabla u) + \rho u(1 - u), \quad (21)$$

with periodic boundary conditions in space, where $D(x, y)$ is the diffusion coefficient, ρ is the reaction rate, and $u : \Omega \rightarrow [0, 1]$ the concentration field. The diffusion coefficient is generated by thresholding a random field with filtered Gaussian frequencies in Fourier space. We consider two cases: one with low frequency modes (case 1) and the one with higher frequencies (case 2), see fig. 6.

A dataset $\mathcal{D} = \{y_{ij}\}_{i,j=1}^{n_x, n_y}$ was generated from measurements of the synthetic field at the final time. Each measurement is assumed to be statistically independent from the others and follows the binomial distribution

$$P(y_{ij}|u_{ij}) = \alpha_{ij}^{y_{ij}} \cdot (1 - \alpha_{ij})^{1-y_{ij}}, \quad (22)$$

where

$$\alpha_{ij} = S\left(\frac{u_{ij} - \tau}{\sigma}\right), \quad S(x) = \frac{1}{1 + e^{-x}}, \quad (23)$$

where τ is a threshold value set to $\tau = 0.5$ and σ the scale of measurement errors. We consider cases with $\sigma = 0.01$ and $\sigma = 0.1$, and show the corresponding data on fig. 6.

We want to infer the initial conditions $u(x, y, 0)$ given this data, and reconstruct the whole concentration field on Ω with uncertainties on the initial conditions. We parameterize the initial conditions as

$$u(x, y, 0) = \exp\left(-\frac{(x - x_0)^2 + (y - y_0)^2}{2R^2}\right), \quad (24)$$

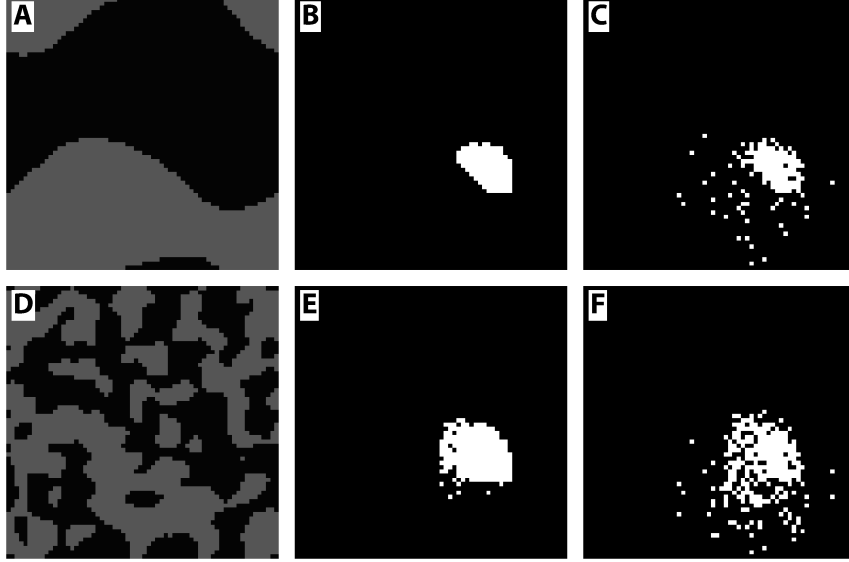


Figure 6: Reaction diffusion data. (A,D) Diffusion field $D(x, y)$ for cases 1 and 2, respectively black and grey regions have values $D = 0.005$ and $D = 0.1$, respectively. (B,C) Data with $\sigma = 0.01$ and $\sigma = 0.05$, respectively, for case 1. (E,F) Data with $\sigma = 0.01$ and $\sigma = 0.05$, respectively, for case 2.

where x_0 and y_0 are the position and R the radius of the initial concentration field. We set $R = L/16$ and want to infer the initial position $\theta = (x_0, y_0)$ with quantified uncertainties using eq. (12).

The log-likelihood of the data is given by

$$\log P(\mathcal{D}|\mathbf{u}) = \sum_{i=1}^{n_x} \sum_{j=1}^{n_y} \log P(y_{ij}|u_{ij}). \quad (25)$$

The dataset \mathcal{D} is synthetically generated for each case using eq. (22) with the numerical solution of eq. (21) at time T , with initial conditions described by eq. (24). The solution is obtained with $\theta_{\text{ref}} = (2L/3, L/3)$, $L = 1$, $T = 0.5$, and $\rho = 8$. The diffusion coefficient takes values $D(x, y) \in \{0.005, 0.1\}$. Finally, we use $n_x = n_y = 64$ points along each spatial dimension and a time step $\Delta t = 6.1 \times 10^{-4}$.

The ODIL solution uses the same spatial resolution as the forward solver, but we use $n_t = 129$ points along the time dimension. The discretization of the PDE employs the midpoint rule in time, and second order finite differences in space. Combining the likelihood, the PDE loss and the loss constraining the initial conditions, the log-posterior of this problem is given by

$$\log P(\mathbf{u}, \theta|\mathcal{D}) = \lambda_{\text{PDE}} n_x n_y n_t L_{\text{PDE}}(\mathbf{u}, \theta) + \lambda_{\text{IC}} n_x n_y L_{\text{IC}}(\mathbf{u}, \theta) + \log P(\mathcal{D}|\mathbf{u}), \quad (26)$$

where $L_{\text{IC}}(\mathbf{u}, \theta)$ is the mean squared error between \mathbf{u} at time 0 and eq. (24) evaluated at the grid points. Finally, we use $\lambda_{\text{PDE}} = 10$ and $\lambda_{\text{IC}} = 100$ for $\sigma = 0.05$, and $\lambda_{\text{PDE}} = 100$ and $\lambda_{\text{IC}} = 1000$ for $\sigma = 0.01$.

We use the Bayesian annealed sequential importance sampling (BASIS) algorithm [50] to sample the posterior distribution of $\theta = (x_0, y_0)$, with parameters $\beta_{\text{BASIS}} = 0.2$, $\gamma_{\text{BASIS}} = 1$, $l_{\text{max}} = 1$ and 256 samples. Each sample is computed with 20000 epochs of the Adam optimizer with learning rate 10^{-3} and required approximately 8 min on a consumer-grade laptop and 2.3 min on a A100 GPU. The posterior distribution of the initial position $\theta = (x_0, y_0)$ given the data is computed for different values of σ in both cases 1 and 2. Samples of these distributions are shown in fig. 7. A higher value of σ means less trust in the data, hence a higher uncertainty in θ . Using samples from these posterior distributions, we can reconstruct the field u_f at

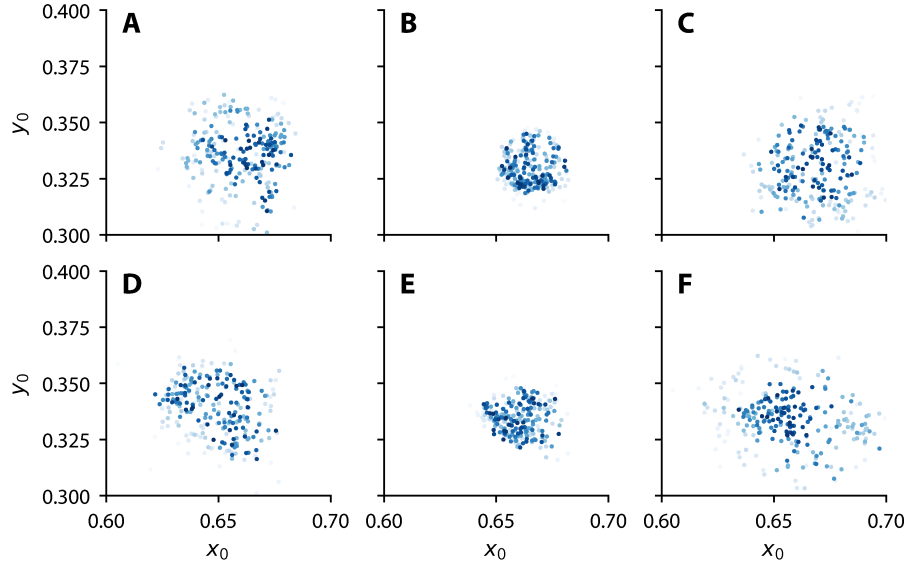


Figure 7: Samples from the posterior distribution of the initial conditions x_0, y_0 obtained with TMCMC. Colors indicate the rank of the log-posterior value of each sample. **(A)** case 1, $\sigma = 0.05$, $\lambda_{\text{PDE}} = 10$, $\lambda_{\text{IC}} = 100$. **(B)** case 1, $\sigma = 0.01$, $\lambda_{\text{PDE}} = 100$, $\lambda_{\text{IC}} = 1000$. **(C)** case 1, $\sigma = 0.01$, $\lambda_{\text{PDE}} = 10$, $\lambda_{\text{IC}} = 100$. **(D)** case 2, $\sigma = 0.05$, $\lambda_{\text{PDE}} = 10$, $\lambda_{\text{IC}} = 100$. **(E)** case 2, $\sigma = 0.01$, $\lambda_{\text{PDE}} = 100$, $\lambda_{\text{IC}} = 1000$. **(F)** case 2, $\sigma = 0.01$, $\lambda_{\text{PDE}} = 10$, $\lambda_{\text{IC}} = 100$.

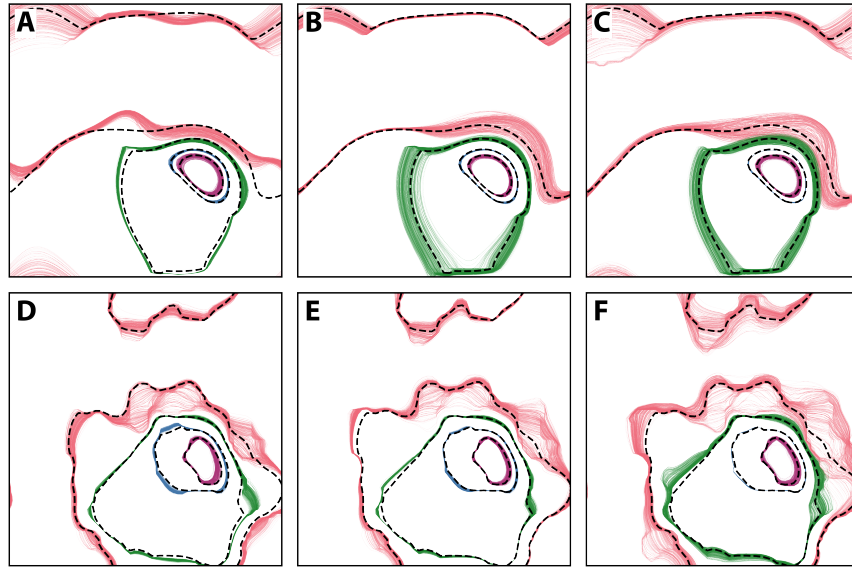


Figure 8: Reconstructed contours of the concentration field from 256 samples of the posterior distribution. Same cases as in fig. 7. The lines corresponds to isocontours of 0.1, 0.3, 0.5 and 0.6 for red, green, blue and magenta, respectively.

$t = T$ and evaluate their uncertainties by using

$$P(u_f|\mathcal{D}) = \int \delta(g(\theta, \mathcal{D}) - u_f) P(\theta|\mathcal{D}) d\theta \approx \frac{1}{K} \sum_{k=1}^K \delta(g(\theta_k, \mathcal{D}) - u_f), \quad \theta_k \sim P(\theta|\mathcal{D}), \quad (27)$$

where $P(\theta|\mathcal{D})$ is the posterior distribution of θ given the data \mathcal{D} , and $g(\theta, \mathcal{D})$ is the ODIL solution of the inverse problem. Contours of the probability density of the concentration field at $t = T$ are shown on fig. 8. In both cases, the predictions are consistent with the ground-truth values, and the uncertainties in the contours are larger when the confidence in the data is lower, i.e. when σ is larger. Furthermore, the reconstruction of the 0.5 contours have a much lower uncertainty than the contours at 0.1 levels. This is consistent with the data being measured around a threshold $\tau = 0.5$, thus the inferred concentration field at time T has much more spatial information around these values.

3.5. Reconstruction of tumor cells concentration in the brain

Medical imaging such as MRI can detect regions on high tumor concentration in the brain, known as gross tumor volume (GTV). However, regions with lower tumor cell density, often containing microscopic signatures of a disease, are not detected using standard imaging modalities. Accurately estimating the full tumor concentration field is essential for developing effective radiation therapy. Recently, a large body of work has focused on biophysical tumor growth models and their use for patient-specific inference from medical imaging. These approaches typically rely on reaction-diffusion or anisotropic diffusion models, sometimes coupled with mass effect, and have been used for tasks such as tumor growth prediction, parameter estimation, and image-based personalization (see e.g., Clatz et al. [51], Hogeia et al. [52, 53], Swanson et al. [54], Biegler et al. [55], Lipková et al. [56], Menze et al. [57], Miniere et al. [58], LaMonica et al. [59] and references therein). The newly introduced method of GliODIL [35] uses ODIL to estimate the tumor concentration satisfying a reaction-diffusion PDE while matching MRI data of brain tumors.

Here we extend this work to estimate uncertainties of the tumor concentration field given observed MRI data of real patients. We then design a clinical target volume (CTV) based on the estimated concentration field. To estimate the concentration field at the time corresponding to the MRI acquisition (time T), GliODIL estimates the density field across the whole time interval $[0, T]$, assuming a small localized tumor at time 0, and assuming that it follows the reaction-diffusion equation

$$\frac{\partial u}{\partial t} = \nabla \cdot (D \nabla u) + \rho u(1 - u), \quad (28)$$

with zero flux at the boundaries of the brain $\nabla u \cdot \mathbf{n} = 0$ on $\partial\Omega$, \mathbf{n} being the normal vector at the brain boundaries. The no-flux condition is enforced by setting the diffusion coefficient D to zero outside brain tissue, so that diffusive fluxes vanish at the interface between brain matter and surrounding regions. Furthermore we assume initial conditions of the form

$$u(x, y, z, 0) = \begin{cases} 0, & u_0(x, y, z) \leq 0.1, \\ 1, & u_0(x, y, z) \geq 1, \\ u_0(x, y, z), & \text{otherwise,} \end{cases} \quad (29)$$

where

$$u_0(x, y, z) = \frac{M}{(4\pi D_t^2)^{3/2}} \exp\left(-\frac{(x-x_0)^2 + (y-y_0)^2 + (z-z_0)^2}{4D_t^2}\right), \quad (30)$$

with fixed values $M = 1500$ and $D_t^2 = 15 \text{ mm}^2$ and initial tumor position (x_0, y_0, z_0) . Furthermore we set the diffusion coefficient as

$$D(x, y, z) = D_g c_g(x, y, z) + D_w c_w(x, y, z), \quad (31)$$

where c_g and c_w are the proportion of gray and white matter, respectively, and D_w and D_g are diffusion coefficient parameters.

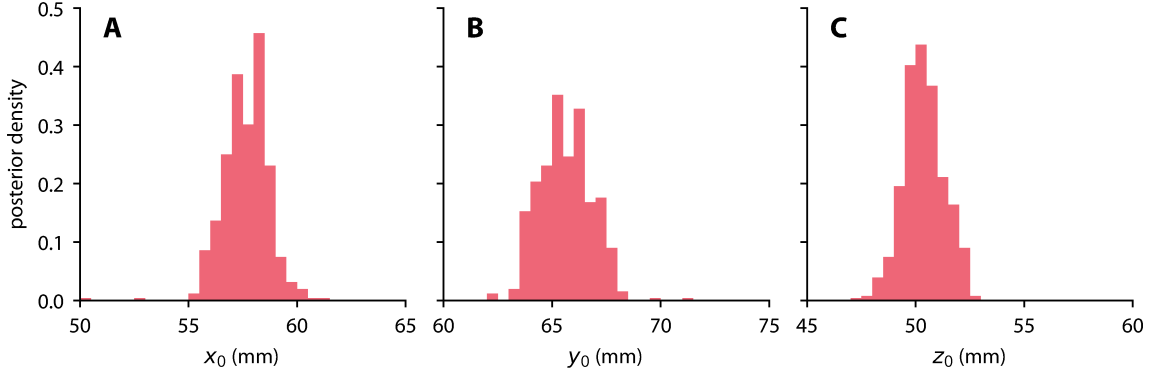


Figure 9: Marginal posterior distribution of the tumor initial position, given the data.

The data corresponds to the segmentation of MRI scans from patients with brain tumors, where each voxel in the brain tissue is classified as belonging to the necrotic core, glioma, or healthy tissue. The data model relates the concentration field u to these classes, and we define the log-likelihood as (see also section Appendix B):

$$\mathcal{L}(\mathcal{D}; \mathbf{u}, \theta) = \frac{1}{\sigma} \sum_{i,j,k} \min(u_{ijk} - \tau_{ijk,lo}, 0) + \min(0, \tau_{ijk,up} - u_{ijk}), \quad (32)$$

where $\sigma = 0.05$ and u_{ijk} is the concentration at voxel indexed by i, j, k . The lower and upper thresholds $\tau_{ijk,lo}$ and $\tau_{ijk,up}$ define an interval for the concentration at each voxel, and are constructed as

$$(\tau_{ijk,lo}, \tau_{ijk,up}) = \begin{cases} (0, \tau_{lo}), & \text{if voxel } ijk \text{ is classified as "healthy",} \\ (\tau_{lo}, \tau_{up}), & \text{if voxel } ijk \text{ is classified as "glioma",} \\ (\tau_{up}, 1), & \text{if voxel } ijk \text{ is classified as "necrotic core",} \end{cases} \quad (33)$$

where $0 < \tau_{lo} < \tau_{up} < 1$ are parameters. The solution u is discretized on a uniform grid that spans a space 50% larger than that spanned by the tumor at time T with $64 \times 64 \times 64$ grid points in space and 128 points in time. Equation (28) is discretized using the Crank-Nicolson scheme, as explained in Balcerak et al. [35] and in section Appendix A.

In addition to the tumor concentration field $u(x, y, z, t)$ over time and space, the parameters of the model and of the initial conditions are inferred: the diffusion coefficient parameters D_w and D_g in white and grey matter, respectively; the reaction rate ρ ; the initial tumor position (x_0, y_0, z_0) ; and the threshold values τ_{lo} and τ_{up} .

With more than 33.4 millions unknowns, estimating the posterior distribution of the whole field and the model parameters would be prohibitively computationally expensive. Thus, we once again use the mode approximation described by eq. (12). Here, we focus on the uncertainties due to the initial tumor position. The overall log-prior corresponding to this problem is given by

$$\log P(\theta|\mathcal{D}) = \arg \min_{\mathbf{u}} (\lambda_{\text{PDE}} n_x n_y n_z n_t L_{\text{PDE}}(\mathbf{u}, \theta) + \lambda_{\text{IC}} n_x n_y n_z L_{\text{IC}}(\mathbf{u}, \theta) + \mathcal{L}(\mathcal{D}; \mathbf{u}, \theta)), \quad (34)$$

with $\lambda_{\text{PDE}} = 10^3$, $\lambda_{\text{IC}} = 200$, of the same order of magnitude than in the original GliODIL implementation [35], and $L_{\text{IC}}(\mathbf{u}, \theta)$ is the mean squared error of the residuals between initial conditions from eq. (29) and the solution \mathbf{u} at $t = 0$.

As in the previous section, we use the BASIS algorithm to create 512 samples from the posterior distribution $P(x_0, y_0, z_0|\mathcal{D})$, with $\beta_{\text{BASIS}} = 0.2$, $\gamma_{\text{BASIS}} = 1.5$, $l_{max} = 1$. For each sample, the optimization is performed over 5000 epochs with the Adam optimizer and a learning rate of 10^{-3} , reduced by half if no

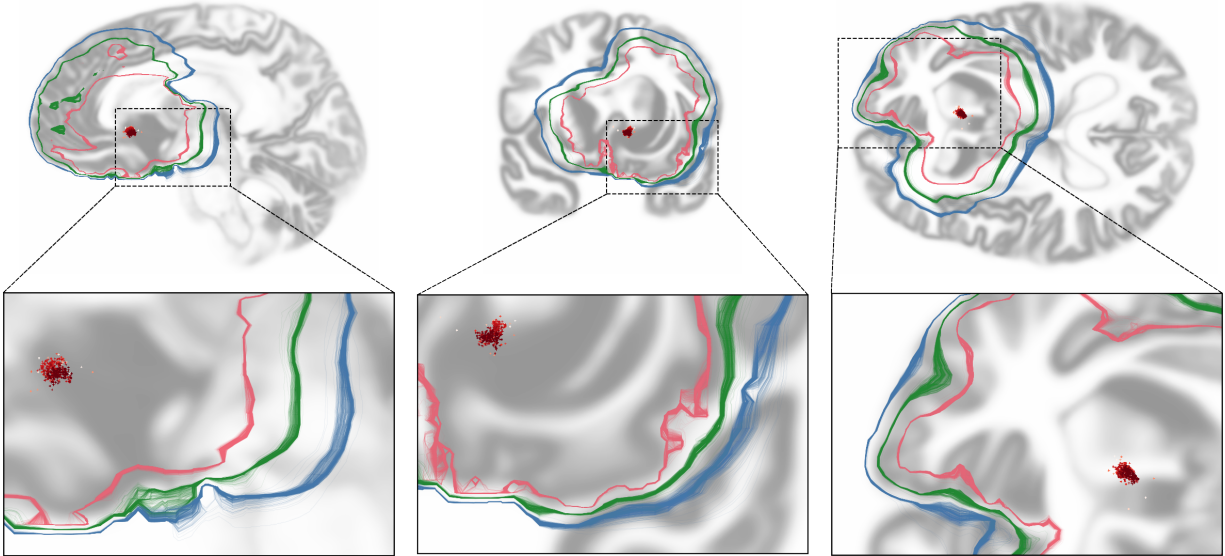


Figure 10: Slice view of the CTVs computed from 256 samples predicted with Gliodil. The CTVs correspond to posterior samples of the initial tumor position, and with the same volume as the standard CTV with margins 1 cm (red), 1.5 cm (green) and 2 cm (blue). Red symbols show the initial position of the tumor sampled from the posterior. Shades of gray indicate the density of gray matter. From left to right: sagittal plane, frontal plane, and transverse plane.

progress was made for 50 consecutive iterations, with a minimal value of 10^{-4} . Each sample is mapped on a H100 GPU and takes about 15 minutes to evaluate. We have used MRI scans that are part of the dataset used in Balcerak et al. [35].

Figure 9 shows histograms of these samples. The initial position inferred by the proposed method is unimodal and concentrated around a position close to the center of mass of the tumor. The uncertainty of the initial position has a spread of about 5 mm, about 5 times the resolution of the MRI scan. This uncertainty is relatively small compared to the size of the tumor.

We now compute the CTV associated with each sample. The CTV is defined as the region enclosed with an isosurface of u and with a given volume. Here we choose volumes of the standard plan with three different margins of 1 cm, 1.5 cm and 2 cm. The CTV of the standard plan is defined as the region within a given margin distance from the segmented necrotic core. Figure 10 shows slices of the CTVs obtained with B-ODIL from the top, front and side views of the brain, going through the center of mass of the necrotic core. We observe a spread of uncertainty of the order of 1 mm to 5 mm, depending on the local properties of brain tissues and on the proximity to boundaries. These findings highlight the ability of the presented Bayesian framework to incorporate spatial uncertainty into CTV estimation in a principled and computationally efficient manner.

4. Summary

We have introduced B-ODIL, a Bayesian extension to ODIL, to solve PDE-based inverse problems with quantified uncertainties. B-ODIL combines prior knowledge in the form of residuals of a PDE with the likelihood function of observed data into a posterior density function of possible solutions. Maximizing this posterior density is equivalent to solving the original ODIL method, making the proposed approach consistent with previous studies. The posterior distribution was estimated through different methods: HMC sampling, Laplace approximation, and a mode approximation that allowed one to estimate the parameters of the model in the context of three dimensional PDE. The Laplace and mode approximations gave consistent

results with the HMC sampling technique, validating their use in higher-dimensional problems where HMC is not feasible.

We have applied B-ODIL to four examples of spatiotemporal PDEs up to four dimensions. In particular, we have estimated uncertainties for three examples with synthetic data and showed that B-ODIL gave consistent results with the ground truth, with high uncertainties in ambiguous regions such as the ill-posed problem of inferring initial conditions in the diffusion equation.

Finally, we have used B-ODIL to estimate the concentration field of tumor cells in the brain of real patients, by combining data from MRI scans with a PDE modeling tumor growth. This application highlights the potential of B-ODIL in a clinical setting, where the quantification of uncertainties is crucial for robust decision-making: providing a distribution of possible tumor fields, rather than a single-point estimate, can inform clinicians about the confidence in the predictions and guide the design of more effective and personalized treatment plans. Furthermore, these results demonstrate that B-ODIL can be applied to real-world problems on a large scale and provides a practical framework for solving PDE-based inverse problems with quantified uncertainties in science and engineering.

Acknowledgments

The computations in this paper were run on the FASRC Cannon cluster supported by the FAS Division of Science Research Computing Group at Harvard University. We thank Sebastian Kaltenebach (Harvard University) and Michal Balcerak (University of Zürich) for their valuable input about Bayesian inference and tumor growth model. This work was supported by the Harvard Data Science Initiative (HDSI) and Amazon Web Services (AWS) under Award Number A59479.

Appendix A. Discretization used in GliODIL

Equation (28) is discretized on a uniform grid with field values $u_{i,j,k}^n$, where n are time indices and i, j , and k are spatial indices. The diffusion and reaction terms are defined as

$$\begin{aligned} A_{i,j,k}^n = & \frac{1}{\Delta x^2} \left(D_{i+\frac{1}{2},j,k}^n (u_{i+1,j,k}^n - u_{i,j,k}^n) - D_{i-\frac{1}{2},j,k}^n (u_{i,j,k}^n - u_{i-1,j,k}^n) \right) \\ & + \frac{1}{\Delta y^2} \left(D_{i,j+\frac{1}{2},k}^n (u_{i,j+1,k}^n - u_{i,j,k}^n) - D_{i,j-\frac{1}{2},k}^n (u_{i,j,k}^n - u_{i,j-1,k}^n) \right) \\ & + \frac{1}{\Delta z^2} \left(D_{i,j,k+\frac{1}{2}}^n (u_{i,j,k+1}^n - u_{i,j,k}^n) - D_{i,j,k-\frac{1}{2}}^n (u_{i,j,k}^n - u_{i,j,k-1}^n) \right), \end{aligned} \quad (\text{A.1})$$

and

$$B_{i,j,k}^n = \rho u_{i,j,k}^n (1 - u_{i,j,k}^n), \quad (\text{A.2})$$

where half indices correspond to the average value of the two adjacent nodes, e.g.

$$D_{i+\frac{1}{2},j,k}^n = \frac{1}{2} (D_{i,j,k}^n + D_{i+1,j,k}^n).$$

The residuals of the discretized equation are computed from the Crank-Nicolson scheme:

$$r_{i,j,k}^n = \frac{u_{i,j,k}^{n+1} - u_{i,j,k}^n}{\Delta t} - \frac{A_{i,j,k}^n + A_{i,j,k}^{n+1}}{2} - \frac{B_{i,j,k}^n + B_{i,j,k}^{n+1}}{2}. \quad (\text{A.3})$$

Appendix B. Log likelihood used in GliODIL

In section 3.5, we have used the log-likelihood described by eq. (32), consistent with the original contribution of GliODIL [35]. Nevertheless, this formulation may appear somewhat arbitrary from a Bayesian inference perspective. Here we show that this formulation is in fact closely related to the likelihood used in section 3.4 for small enough values of σ .

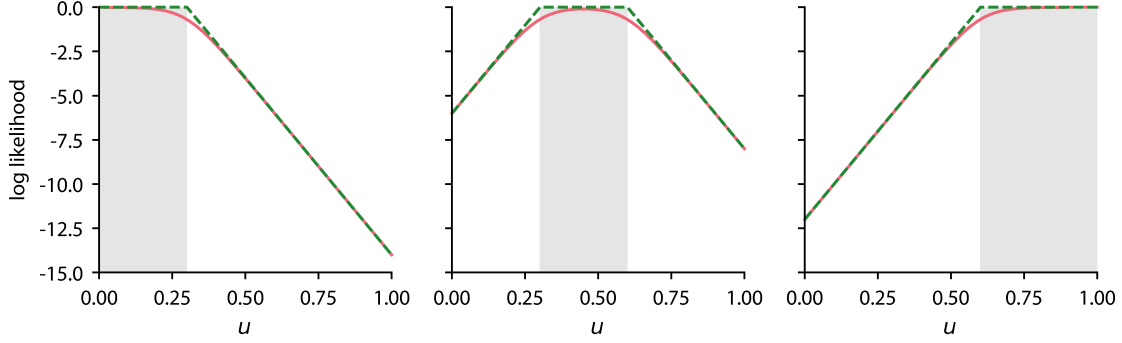


Figure B.11: Log-likelihood for a single voxel to be classified as healthy (left), glioma (middle), or necrotic core (right), against u , with $(\tau_{lo}, \tau_{hi}) = (0.3, 0.6)$ and $\sigma = 0.05$. Shaded regions show the intervals $(\tau_{ijk,lo}, \tau_{ijk,hi})$. Dashed line is the log-likelihood computed in GliODIL (see eq. (32)), and the solid line represents the log-likelihood described by eq. (B.1).

We generalize the likelihood described in section 3.4 to the case of three classes in the segmented data: healthy, glioma, and necrotic core. Each class corresponds to a range of tumor concentration. We consider that voxels are independent from each other, and that the probability of each class is given by

$$\begin{aligned}
 P(\text{healthy}|u) &= \frac{1}{Z(u)} S\left(\frac{\tau_{lo} - u}{\sigma}\right), \\
 P(\text{glioma}|u) &= \frac{1}{Z(u)} S\left(\frac{\tau_{up} - u}{\sigma}\right) \cdot S\left(\frac{u - \tau_{lo}}{\sigma}\right), \\
 P(\text{necrotic core}|u) &= \frac{1}{Z(u)} S\left(\frac{u - \tau_{up}}{\sigma}\right),
 \end{aligned} \tag{B.1}$$

where S is the sigmoid function defined in eq. (23) and $Z(u)$ is the normalization factor

$$Z(u) = 1 + S\left(\frac{u - \tau_{up}}{\sigma}\right) \cdot S\left(\frac{\tau_{lo} - u}{\sigma}\right).$$

Figure B.11 compares this expression with eq. (32) for $\sigma = 0.05$. Both expressions have very similar values, except for a smoother transition near τ_{lo} and τ_{up} for eq. (B.1). In this work we have used the simpler form described by eq. (32) to be consistent with the original GliODIL formulation.

References

- [1] O. Ghattas, K. Willcox, Learning physics-based models from data: perspectives from inverse problems and model reduction, *Acta Numerica* 30 (2021) 446–551. doi:10.1017/S0962492921000064.
- [2] H. Gunes, U. Rist, On the use of kriging for enhanced data reconstruction in a separated transitional flat-plate boundary layer, *Physics of Fluids* 20 (2008).
- [3] Y. Ding, Z. Li, Z. Chen, Y. Ji, J. Yu, J. Ye, Full-volume 3d fluid flow reconstruction with light field piv, *IEEE transactions on pattern analysis and machine intelligence* 45 (2023) 8405–8418.
- [4] P. Karnakov, S. Litvinov, P. Koumoutsakos, Flow reconstruction by multiresolution optimization of a discrete loss with automatic differentiation, *The European Physical Journal E* 46 (2023) 59.
- [5] A. Carrassi, M. Bocquet, L. Bertino, G. Evensen, Data assimilation in the geosciences: An overview of methods, issues, and perspectives, *Wiley Interdisciplinary Reviews: Climate Change* 9 (2018) e535.

- [6] P. Suetens, *Fundamentals of medical imaging*, Cambridge university press, 2017.
- [7] K. H. Jin, M. T. McCann, E. Froustey, M. Unser, Deep convolutional neural network for inverse problems in imaging, *IEEE transactions on image processing* 26 (2017) 4509–4522.
- [8] P. Angelikopoulos, C. Papadimitriou, P. Koumoutsakos, Bayesian uncertainty quantification and propagation in molecular dynamics simulations: a high performance computing framework, *The Journal of chemical physics* 137 (2012).
- [9] A. Economides, G. Arampatzis, D. Alexeev, S. Litvinov, L. Amoudruz, L. Kulakova, C. Papadimitriou, P. Koumoutsakos, Hierarchical bayesian uncertainty quantification for a model of the red blood cell, *Physical Review Applied* 15 (2021) 034062.
- [10] L. Amoudruz, A. Economides, G. Arampatzis, P. Koumoutsakos, The stress-free state of human erythrocytes: Data-driven inference of a transferable rbc model, *Biophysical Journal* 122 (2023) 1517–1525.
- [11] V. Isakov, *Inverse problems for partial differential equations*, Springer, 2006.
- [12] D. Galbally, K. Fidkowski, K. Willcox, O. Ghattas, Nonlinear model reduction for uncertainty quantification in large-scale inverse problems, *International Journal for Numerical Methods in Engineering* 81 (2010) 1581–1608. doi:10.1002/nme.2778.
- [13] C. Lieberman, K. Willcox, O. Ghattas, Parameter and state model reduction for large-scale statistical inverse problems, *SIAM Journal on Scientific Computing* 32 (2010) 2523–2542. doi:10.1137/090775622.
- [14] A. M. Stuart, *Inverse problems: a bayesian perspective*, *Acta numerica* 19 (2010) 451–559.
- [15] A. Tarantola, *Inverse problem theory and methods for model parameter estimation*, SIAM, 2005.
- [16] O. Scherzer, M. Grasmair, H. Grossauer, M. Haltmeier, F. Lenzen, *Variational methods in imaging*, volume 167, Springer, 2009.
- [17] M. A. Iglesias, A regularizing iterative ensemble kalman method for pde-constrained inverse problems, *Inverse Problems* 32 (2016) 025002.
- [18] T. van Leeuwen, F. J. Herrmann, A penalty method for pde-constrained optimization in inverse problems, *Inverse Problems* 32 (2015) 015007.
- [19] T. Bui-Thanh, O. Ghattas, J. Martin, G. Stadler, A computational framework for infinite-dimensional bayesian inverse problems part i: The linearized case, with application to global seismic inversion, *SIAM Journal on Scientific Computing* 35 (2013) A2494–A2523.
- [20] N. Petra, J. Martin, G. Stadler, O. Ghattas, A computational framework for infinite-dimensional bayesian inverse problems, part ii: Stochastic newton mcmc with application to ice sheet flow inverse problems, *SIAM Journal on Scientific Computing* 36 (2014) A1525–A1555.
- [21] H. Antil, A. K. Saibaba, Efficient algorithms for bayesian inverse problems with whittle–matérn priors, *SIAM Journal on Scientific Computing* 46 (2024) S176–S198.
- [22] L. Lu, P. Jin, G. Pang, Z. Zhang, G. E. Karniadakis, Learning nonlinear operators via deepnet based on the universal approximation theorem of operators, *Nature machine intelligence* 3 (2021) 218–229.
- [23] Z. Li, N. Kovachki, K. Azizzadenesheli, B. Liu, K. Bhattacharya, A. Stuart, A. Anandkumar, Fourier neural operator for parametric partial differential equations, *arXiv preprint arXiv:2010.08895* (2020).
- [24] H. Gao, M. J. Zahr, J.-X. Wang, Physics-informed graph neural galerkin networks: A unified framework for solving pde-governed forward and inverse problems, *Computer Methods in Applied Mechanics and Engineering* 390 (2022) 114502.

- [25] G. Duthé, I. Abdallah, E. Chatzi, Graph transformers for inverse physics: reconstructing flows around arbitrary 2d airfoils, arXiv preprint arXiv:2501.17081 (2025).
- [26] Z. Zou, X. Meng, A. F. Psaros, G. E. Karniadakis, Neuraluq: A comprehensive library for uncertainty quantification in neural differential equations and operators, SIAM Review 66 (2024) 161–190.
- [27] R. Molinaro, Y. Yang, B. Engquist, S. Mishra, Neural inverse operators for solving pde inverse problems, arXiv preprint arXiv:2301.11167 (2023).
- [28] S. Kaltenbach, P. Perdikaris, P.-S. Koutsourelakis, Semi-supervised invertible deepnets for bayesian inverse problems, stat 1050 (2022) 8.
- [29] J. Adler, O. Öktem, Deep bayesian inversion, arXiv preprint arXiv:1811.05910 (2018).
- [30] M. Raissi, P. Perdikaris, G. E. Karniadakis, Physics-informed neural networks: A deep learning framework for solving forward and inverse problems involving nonlinear partial differential equations, Journal of Computational physics 378 (2019) 686–707.
- [31] P. Karnakov, S. Litvinov, P. Koumoutsakos, Solving inverse problems in physics by optimizing a discrete loss: Fast and accurate learning without neural networks, PNAS nexus 3 (2024) pgae005.
- [32] S. Cai, Z. Mao, Z. Wang, M. Yin, G. E. Karniadakis, Physics-informed neural networks (pinns) for fluid mechanics: A review, Acta Mechanica Sinica 37 (2021) 1727–1738.
- [33] A. B. Buhendwa, D. A. Bezgin, P. Karnakov, N. A. Adams, P. Koumoutsakos, Data-driven shape inference in three-dimensional steady-state supersonic flows: Optimizing a discrete loss with jax-fluids, Physical Review Fluids 10 (2025) 084902.
- [34] C. Scott, Using scientific machine learning to enhance measurements of 2D turbulent flows with mODIL, in: 2024 Regional Student Conferences, 2024, p. 90557.
- [35] M. Balcerak, J. Weidner, P. Karnakov, I. Ezhov, S. Litvinov, P. Koumoutsakos, R. Z. Zhang, J. S. Lowengrub, B. Wiestler, B. Menze, Individualizing glioma radiotherapy planning by optimization of data and physics-informed discrete loss, Nature Communications 16 (2025) 5982.
- [36] M. Balcerak, T. Amiranashvili, A. Wagner, J. Weidner, P. Karnakov, J. C. Paetzold, I. Ezhov, P. Koumoutsakos, B. Wiestler, et al., Physics-regularized multi-modal image assimilation for brain tumor localization, Advances in Neural Information Processing Systems 37 (2024) 41909–41933.
- [37] P. Karnakov, L. Amoudruz, P. Koumoutsakos, Optimal navigation in microfluidics via the optimization of a discrete loss, Physical Review Letters 134 (2025) 044001.
- [38] L. Amoudruz, P. Karnakov, P. Koumoutsakos, Contactless precision steering of particles in a fluid inside a cube with rotating walls, Journal of Fluid Mechanics 1014 (2025) A15.
- [39] L. Yang, X. Meng, G. E. Karniadakis, B-pinns: Bayesian physics-informed neural networks for forward and inverse pde problems with noisy data, Journal of Computational Physics 425 (2021) 109913.
- [40] A. S. Nair, B. Jacob, A. A. Howard, J. Drgona, P. Stinis, E-pinns: Epistemic physics-informed neural networks, arXiv preprint arXiv:2503.19333 (2025).
- [41] Y. Yu, C. H. Ho, Y. Wang, A conformal prediction framework for uncertainty quantification in physics-informed neural networks, arXiv preprint arXiv:2509.13717 (2025).
- [42] A. Paszke, S. Gross, F. Massa, A. Lerer, J. Bradbury, G. Chanan, T. Killeen, Z. Lin, N. Gimelshein, L. Antiga, et al., Pytorch: An imperative style, high-performance deep learning library, Advances in neural information processing systems 32 (2019).

- [43] S. L. Cotter, G. O. Roberts, A. M. Stuart, D. White, Mcmc methods for functions: modifying old algorithms to make them faster, *Statistical Science* (2013) 424–446.
- [44] L. Tierney, J. B. Kadane, Accurate approximations for posterior moments and marginal densities, *Journal of the american statistical association* 81 (1986) 82–86.
- [45] R. E. Morrison, T. A. Oliver, R. D. Moser, Representing model inadequacy: A stochastic operator approach, *SIAM/ASA Journal on Uncertainty Quantification* 6 (2018) 457–496.
- [46] Z. Wang, R. Ghanem, Stochastic modeling and statistical calibration with model error and scarce data, *Computer Methods in Applied Mechanics and Engineering* 416 (2023) 116339.
- [47] D. P. Kingma, Adam: A method for stochastic optimization, *arXiv preprint arXiv:1412.6980* (2014).
- [48] R. M. Neal, et al., Mcmc using hamiltonian dynamics, *Handbook of markov chain monte carlo* 2 (2011) 2.
- [49] D. C. Liu, J. Nocedal, On the limited memory bfgs method for large scale optimization, *Mathematical programming* 45 (1989) 503–528.
- [50] S. Wu, P. Angelikopoulos, C. Papadimitriou, P. Koumoutsakos, Bayesian annealed sequential importance sampling: an unbiased version of transitional markov chain monte carlo, *ASCE-ASME Journal of Risk and Uncertainty in Engineering Systems, Part B: Mechanical Engineering* 4 (2018) 011008.
- [51] O. Clatz, M. Sermesant, P.-Y. Bondiau, H. Delingette, S. K. Warfield, G. Malandain, N. Ayache, Realistic simulation of the 3-d growth of brain tumors in mr images coupling diffusion with biomechanical deformation, *IEEE transactions on medical imaging* 24 (2005) 1334–1346.
- [52] C. Hoguea, G. Biros, F. Abraham, C. Davatzikos, A robust framework for soft tissue simulations with application to modeling brain tumor mass effect in 3d mr images, *Physics in Medicine & Biology* 52 (2007) 6893.
- [53] C. Hoguea, C. Davatzikos, G. Biros, An image-driven parameter estimation problem for a reaction–diffusion glioma growth model with mass effects, *Journal of mathematical biology* 56 (2008) 793–825.
- [54] K. R. Swanson, E. C. Alvord Jr, J. Murray, Quantifying efficacy of chemotherapy of brain tumors with homogeneous and heterogeneous drug delivery, *Acta biotheoretica* 50 (2002) 223–237.
- [55] L. Biegler, G. Biros, O. Ghattas, M. Heinkenschloss, D. Keyes, B. Mallick, L. Tenorio, B. van Bloemen Waanders, K. Willcox, Y. Marzouk, *Large-scale inverse problems and quantification of uncertainty*, volume 712, Wiley Online Library, 2010.
- [56] J. Lipková, P. Angelikopoulos, S. Wu, E. Alberts, B. Wiestler, C. Diehl, C. Preibisch, T. Pyka, S. E. Combs, P. Hadjidoukas, et al., Personalized radiotherapy design for glioblastoma: integrating mathematical tumor models, multimodal scans, and bayesian inference, *IEEE transactions on medical imaging* 38 (2019) 1875–1884.
- [57] B. H. Menze, A. Jakab, S. Bauer, J. Kalpathy-Cramer, K. Farahani, J. Kirby, Y. Burren, N. Porz, J. Slotboom, R. Wiest, et al., The multimodal brain tumor image segmentation benchmark (brats), *IEEE transactions on medical imaging* 34 (2014) 1993–2024.
- [58] H. J. Miniere, D. A. Hormuth, E. A. Lima, M. Farhat, B. Panthi, H. Langshaw, M. D. Shanker, W. Talpur, S. Thrower, J. Goldman, et al., A data assimilation framework for predicting the spatiotemporal response of high-grade gliomas to chemoradiation, *BMC cancer* 25 (2025) 1239.
- [59] M. F. LaMonica, T. E. Yankeelov, D. A. Hormuth, Investigating the limits of predictability of magnetic resonance imaging-based mathematical models of tumor growth, *Cancers* 17 (2025) 3361.